INTERNATIONAL JOURNAL OF ENERGY STUDIES

e-ISSN: 2717-7513 (ONLINE); homepage: https://dergipark.org.tr/en/pub/ijes

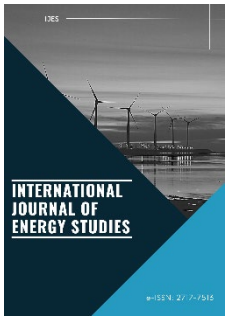

Research Article

Int J Energy Studies 2026; 11(2): 1531-1552

DOI: 10.58559/ijes.1701802

Received : 19 May 2025

Revised : 10 Jun 2025

Accepted : 03 Feb 2026

Experimental and numerical analysis of energy and hydrodynamic pressure in channel flow induced through a water wave generation system

Gulenay Alevay Kilic [a*], Batin Demircan [b], Nuray Gedik [c], Altug Yavas [d]

[a]*Department of Electrical and Energy, Yalova Vocational School, Yalova University, Yalova, 77200, Türkiye, ORCID : 0000-0002-3513-8785*

[b]*Department of Electronics and Automation, Balıkesir Vocational School, Balikesir University, Balıkesir, Türkiye, ORCID : 0000-0002-0765-458X*

[c] *Department of Civil Engineering, Balikesir University, Balikesir 10145, Türkiye, ORCID : 0000-0002-5070-4642*

[d] *Department of Civil Engineering, Balikesir University, Balikesir 10145, Türkiye, ORCID : 0000-0002-2619-8671*

*(*Corresponding Author: gulenay.kilic@yalova.edu.tr)*

Highlights

- A remarkably high agreement rate of 94% was achieved between the experimentally generated regular wave and the numerical simulations.
- URANS approach and SST k-ω model successfully represented pre-breaking energy concentrations.
- Subsurface pressure and velocity gradients were observed to influence the distribution of energy intensity.
- The pressure-based analysis provided more comprehensive results compared to classical surface-based approaches.
- The findings offer decision support for efficiency evaluation and engineering design in the implementation of wave energy systems.

You can cite this article as: Kilic GA, Demircan B, Gedik N, Yavas A. Experimental and numerical analysis of energy and hydrodynamic pressure in channel flow induced through a water wave generation system. Int J Energy Studies 2026; 11(2): 1531-1552

ABSTRACT

Wave energy has been gaining increasing significance among renewable energy sources due to its continuity and predictable nature. In engineering applications within this field, it is essential to evaluate not only free surface behavior but also subsurface flow structures, pressure gradients (∇Ps), and acceleration fields. In the experimental setup, wave surface elevations generated by a hydraulic servo system (HSS) with a stroke length of 50 mm and a frequency of 1 Hz were recorded in real-time at 0.1 ms intervals using a wave probe. Additionally, the measured free surface wave behavior was compared with numerical results obtained through three-dimensional (3D) computational fluid dynamics (CFD) analysis. The numerical simulations were conducted using the volume of fluid (VOF) method and the SST k-ω turbulence model based on the Unsteady Reynolds-Averaged Navier–Stokes (URANS) approach in ANSYS Fluent 2023 R2. The inlet boundary conditions were defined as time-dependent through a user-defined function (UDF). A convergence rate of approximately 94% was achieved between the experimental and numerical free surface elevations. Velocity fields (m/s), static and dynamic pressure contours (Pa), and pressure gradient (∇P) (Pa/m) distributions obtained from the numerical model were analyzed in detail. The findings indicate the formation of energy accumulation zones during wave crest-trough transitions and reveal increased load transfers associated with subsurface load distributions and acceleration.

Keywords: Wave energy, CFD, renewable energy, hydrodynamics

1. INTRODUCTION

Wave energy is considered more reliable than solar or wind power in certain regions due to the continuous generation of waves driven by wind and currents, allowing utilization up to 90% of the time. This results in a high energy density per unit area [1,2]. In the context of the growing global demand for clean and sustainable energy sources, wave energy has emerged as a promising alternative to fossil fuels [3]. Wave energy converters (WECs) are specifically designed to harness the natural motion of ocean waves for electricity generation [4–7]. In laboratory-scale studies, wave channels are commonly used to simulate wave conditions, where piston- and flap-type wave makers are employed to generate controlled wave motions.

In recent years, advancements in numerical modeling and CFD software have provided solutions with accuracy levels that can potentially replace experimental methods in coastal and ocean engineering applications. Modeling of renewable energy resources such as wave energy has become one of the most prominent applications of these numerical approaches [8].

Machado et al. (2018) simulated the generation and propagation of regular waves in a numerical wave tank developed using ANSYS CFX and demonstrated that piston-type wave makers yielded more stable and theoretically consistent results. To reduce wave reflections, a sloped beach and time-controlled boundary conditions were implemented at the end of the channel, and the results showed high agreement with second-order Stokes theory. The study contributes to enhancing the accuracy of wave generation in numerical environments and to the reliable modeling of wave-induced pressure distributions [9].

Velioglu Sogut et al. (2021) experimentally and numerically investigated the interaction of solitary waves with steady currents in a macro-roughened environment using LES-based methods. The study revealed that wave–current interaction significantly affects the local flow regime and the horizontal/vertical velocity components. The application of Froude similarity and a VOF-based solution approach was found to play a critical role in accurately representing the physical process [10].

Accurate modeling of wave-induced currents requires the physical representation of turbulence structures beneath the free surface. As emphasized in the study by Larsen and Fuhrman (2023), classical two-equation turbulence models (e.g., the standard k-ω model) tend to overproduce

turbulence energy, leading to erroneous predictions of flow structures and, consequently, transport behavior. The stabilized k-ω approach proposed in their study suppresses turbulence growth prior to wave breaking, thereby providing a more accurate hydrodynamic representation [11]. Yin et al. (2024) analyzed breaking-influenced wave propagation over sloped surfaces using a stabilized k-ω SST model and developed empirical models for drag coefficient (CD) estimation based on Reynolds and Iribarren numbers. This study highlights the impact of wave breaking on hydrodynamic resistance parameters [12]. Under low-energy sea conditions, due to the limited kinetic energy of surface waves, wave-induced pressure distribution becomes a critical parameter in determining energy conversion efficiency. According to Airy theory, although pressure fluctuations decrease with depth, this attenuation varies depending on the wavelength and water depth. Particularly in shallow waters, pressure effects near the seabed can directly influence the performance of converter systems. In this context, accurately modeling the pressure profile around the buoy is essential for enhancing energy efficiency [13–14].

Moreover, wave steepness has emerged as a more decisive parameter than significant wave height or energy period in determining the optimum accumulator pressure in hydraulic PTO systems. This not only simplifies the design process but also improves energy conversion performance [15]. Stokes drift observed in irrotational wave systems induces net mass transport in the direction of wave propagation, contributing to both material transport and average pressure–momentum transfer. This enables more accurate modeling of energy interactions within a Lagrangian framework [16]. Similarly, in two-layer systems such as the Istanbul Strait, the hydrostatic pressure difference between seas is the primary driver of bidirectional flow and interfacial mixing. In such systems, pressure-based modeling proves effective in explaining stratified flow dynamics and associated transport processes [17].

In recent years, FPGA-based control systems have become a preferred method for the real-time control of nonlinear hydraulic and mechatronic systems due to their high sampling frequency, low latency, and deterministic processing capabilities. However, in the literature, studies that experimentally and numerically investigate the impact of these hardware advantages on wave generation—particularly on time-dependent pressure distributions—remain limited. Under low-energy sea conditions, the pressure distribution between wave troughs and crests directly affects the dynamic performance of wave energy systems. In this study, high-resolution CFD analyses of subsurface ∇Ps are conducted using a 3D URANS formulation and an enhanced

SST k-ω turbulence model, aiming to improve the physical representation of the pressure–momentum relationship in wave energy conversion processes. In the efficiency optimization of wave energy systems, the temporal and spatial variation of pressure fields occurring during crest–trough transitions and pre-breaking zones is of critical importance. Detailed numerical resolution of these regions provides directly translatable quantitative data for identifying energy concentration zones—surpassing the limitations of classical surface-based approaches and informing design processes more effectively.

2. EXPERIMENTAL AND NUMERICAL FRAMEWORK

2.1. Experimental Setup

A hydraulic servo system (HSS) with a double-acting, double-rod configuration was employed to drive the piston-type wave generator in the wave channel. In this study, the HSS enables the piston-type wave maker (PTWM) to operate with a stroke length of 50 mm. The proportional directional control valve (PDV) integrated into the HSS allows proportional adjustment of the HSS movement in both forward and backward directions. Passive wave absorbers were installed behind the PTWM and at the downstream end of the wave channel to prevent reflected waves generated after wave formation. The overall structure of the wave channel is illustrated in Figure 1.

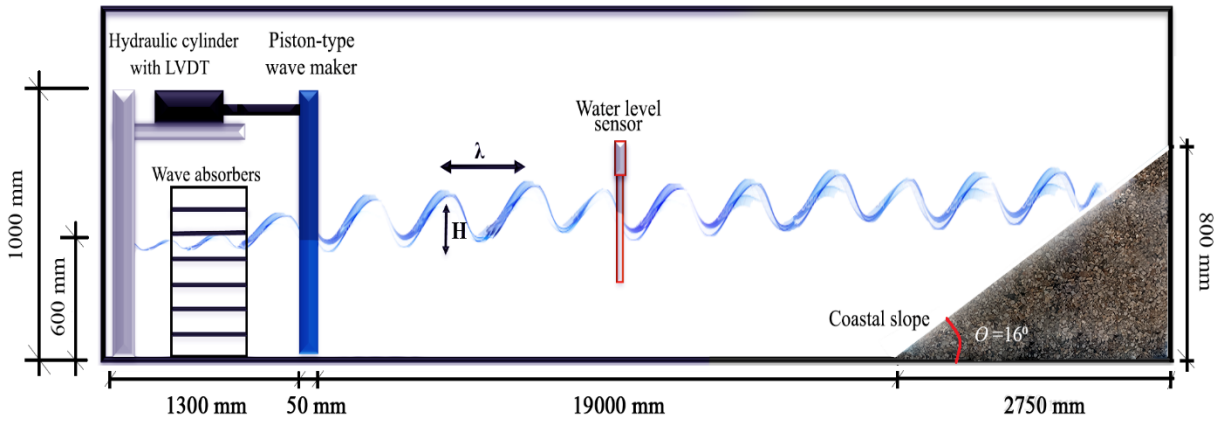

Figure 1. The structure of the wave channel, not drawn to scale.

The PTWM structure was positioned using a linear rail system mounted on the wave channel and a supporting frame located outside the channel, thereby minimizing the physical impact of the wave generator's weight on the channel itself. Detailed views of the PTWM structure are presented in Figure 2.

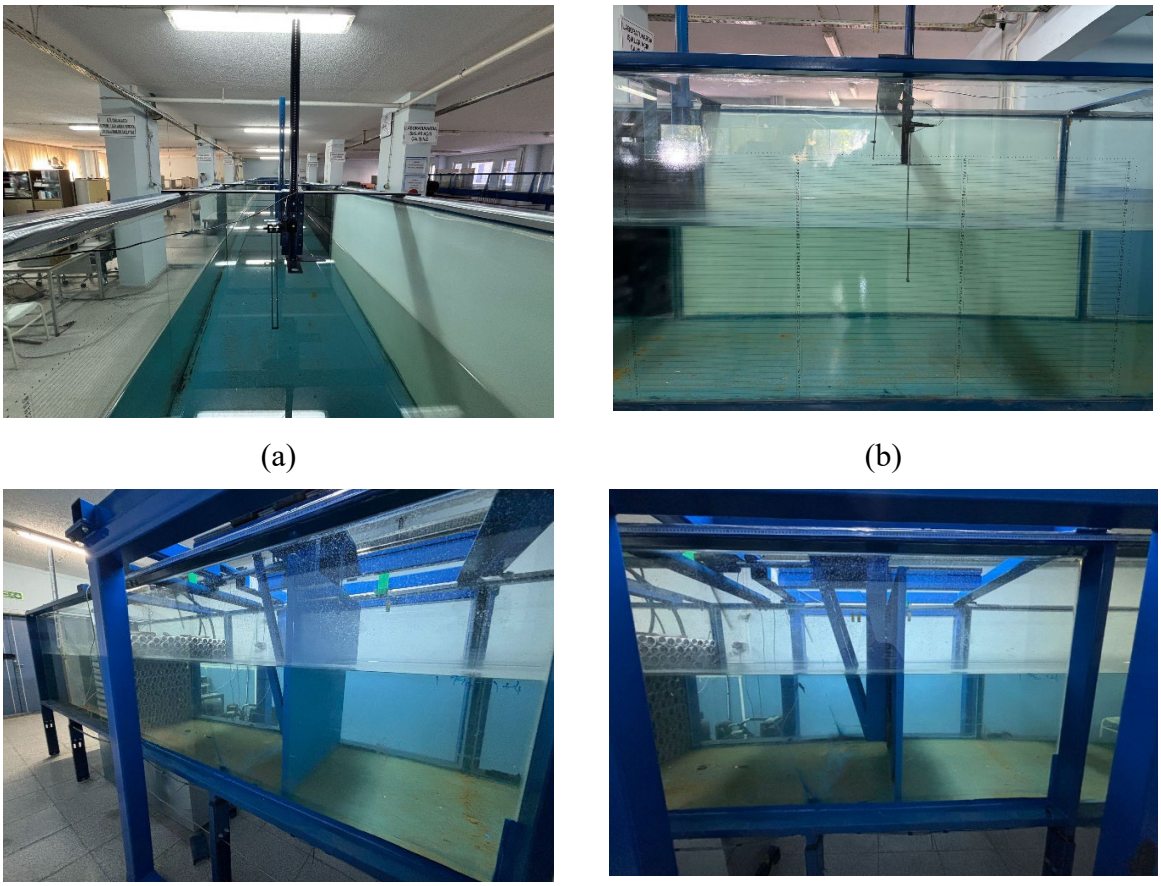

(a) (b)

(c) (d)

Figure 2. Deney seti: (a) kanalın görünüşü (b) sensörün bulunduğu konum (a) view of the wave maker (c) isometric view of the wave maker(d) right plane view of the wave maker

The waves generated in the wave channel propagate unidirectionally along the channel. Upon reaching the end of the channel, these waves collide with the channel wall and subsequently generate reflected waves after a certain period. To minimize the effect of wave reflections, a coastal-type wave absorber with a 16% slope was employed. For real-time visualization and monitoring of the waves produced in the channel, measurements were performed using a wave probe positioned 10 meters from the PTWM's resting position along the channel. The wave probe used for measurement operated within a range of ±10 V, with a sampling frequency of 50 Hz and a resolution of 15 bits.

2.2. Wave channel controller hardware

Position measurements within the wave generation system utilized in this study were carried out using a Linear Variable Differential Transformer (LVDT) sensor. The analog signals obtained from the sensor were transmitted to the controller via the NI-9215 analog input module. The

control architecture was built around the NI cRIO-9074 compact embedded controller, which is equipped with a 400 MHz Freescale MPC5200 real-time processor, a Xilinx Spartan-3 FPGA, 128 MB of DRAM, and 256 MB of flash memory. Operating on the NI Real-Time platform, the system supports programming environments including LabVIEW, C/C++, and the NI Scan Engine.

The Field Programmable Gate Array (FPGA) integrated within the device provides a suitable hardware platform for high-precision and customizable control applications, owing to its parallel processing capabilities. The FPGA module was programmed directly using control algorithms developed in the NI LabVIEW environment.

To enable precise control of the hydraulic system's stroke motion within a defined range, a sinusoidal reference signal was generated in the LabVIEW FPGA environment. The amplitude and frequency parameters of this signal were defined by the user through a LabVIEW-based interface, allowing the system to track the specified reference position signal. The control signal was transmitted to the Position-Controlled Directional Valve (PDV) via the NI-9263 analog output module, while the position data from the LVDT sensor were delivered to the system through the NI-9215 analog input module. Both the reference and feedback signals were directly routed to the FPGA module to enable real-time control.

In addition, analog signals obtained from the measurement probe placed in the wave channel were also transmitted to the FPGA via the NI-9215 module. The overall control architecture of the FPGA-based wave generation system is presented in Figure 3.

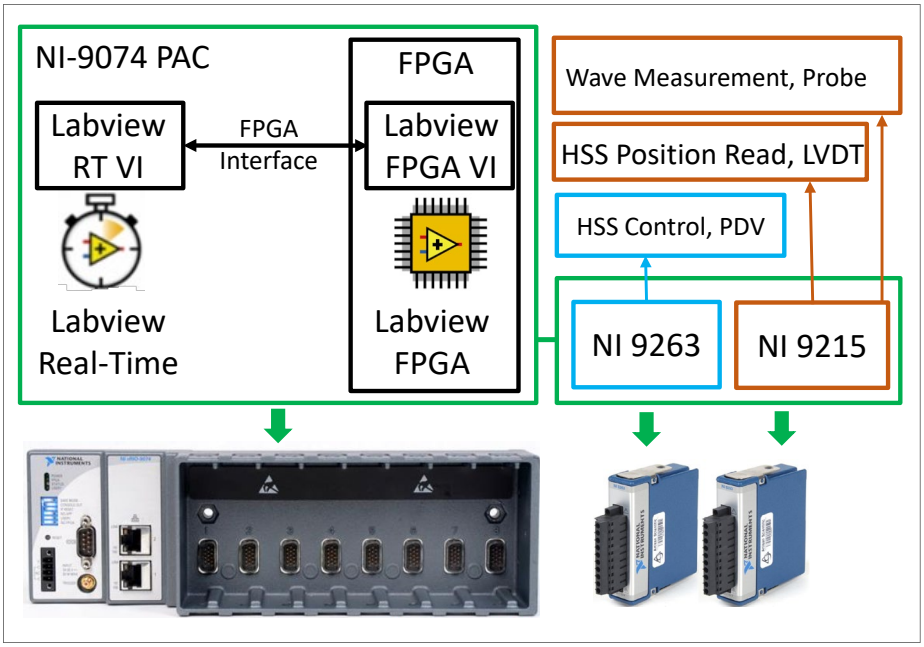

Figure 3. General structure of wave generating system

2.3. Numerical Setup and Validation

The numerical analyses were configured to correspond with the experimental setup, based on identical geometric structures, boundary conditions, and flow parameters. A Volume of Fluid (VOF) method was applied for the Eulerian approach to solving free-surface, two-phase flows through three-dimensional modeling. The model accounted for surface tension effects, interphase momentum transfer, and turbulence characteristics. Calculations were carried out using ANSYS Fluent 2023 R2, with the computational mesh, time step, and convergence criteria defined based on numerical stability and solution accuracy. The surface elevation profiles obtained from the simulations were compared with experimental data to evaluate the accuracy of the model. Based on these parameters, the hydrodynamic behavior of the system was assessed in a dimensionless framework.

2.4. Flow governing equations and interface modeling

In this study, the Volume of Fluid (VOF) method was employed to model free-surface multiphase flows. The VOF approach enables sharp tracking of the interface between immiscible phases while numerically preserving the principle of mass conservation. The continuity equation is expressed in terms of the mixture density (ρ_m) and mass-averaged velocity ($\vec{v}_m$), defined based on local densities and volumetric fractions, thus ensuring compliance with the incompressibility condition [12, 18–19].

The momentum equation was formulated using the mixture approach, in which the cumulative effects of all phases are considered collectively. The equation accounts for ∇Ps, viscous stresses, gravitational acceleration, and interfacial forces between phases. Additionally, drift velocities associated with secondary phases are incorporated into the momentum transfer formulation. The momentum equation for the mixture is derived by summing the individual momentum equations of all phases and is expressed in Equation (1) [18].

$$\frac{\partial}{\partial t}\left(\rho_m \vec{v}_m\right) + \nabla.\left(\rho_m \vec{v}_m \vec{v}_m\right) = -\nabla \mathrm{p} + \nabla.\left[\mu_m\left(\nabla \vec{v}_m + \vec{v}_m^T\right)\right] + \rho_m \vec{g} + \vec{F} - \nabla.\left(\sum_{k=1}^{n} \alpha_k \rho_k \vec{v}_{dr,k}\, \vec{v}_{dr,k}\right) \tag{1}$$

Where k is the number of phases, is a body force.

The energy equation was employed to represent the thermodynamic behavior within the system. This equation encompasses temperature distribution, conduction, diffusion, and viscous dissipation effects. In the energy formulation, the total energy of each phase consists of specific enthalpy, pressure–volume work, and kinetic energy components. For incompressible phases, only the enthalpy term is considered, whereas for compressible phases, the relationship between pressure and density is also taken into account. The energy equation for the mixture is expressed by Equation (2) [18]:

$$\frac{\partial}{\partial t}\sum_k\left(\alpha_k \rho_k E_k\right) + \nabla.\sum_k\left(\alpha_k \vec{v}_k\left(\rho_k E_k + p\right)\right) = \nabla.\left(k_{eff}\nabla \mathrm{T} - \sum_k\sum_k h_{j,k}\vec{J}_{j,k} + \left(\bar{\bar{\tau}}_{eff} * \vec{v}\right)\right) + S_h \tag{2}$$

α_k is the volume fraction of phase k. To accurately resolve the dynamic behavior of free-surface multiphase flows, the momentum transport equations for each phase must be addressed through an integrated approach. In this context, the momentum equation in systems defined by the Volume of Fluid (VOF) method is formulated to include key physical components such as ∇Ps, viscous stresses, gravitational effects, and interfacial forces between phases. The momentum equation for the mixture is obtained by summing the individual momentum equations of all phases and is presented as Equation (3) [18].

$$\frac{\partial}{\partial t}\left(\rho_m \vec{v}_m\right) + \nabla.\left(\rho_m \vec{v}_m \vec{v}_m\right) = -\nabla \mathrm{p} + \nabla.\left[\mu_m\left(\nabla \vec{v}_m + \vec{v}_m^T\right)\right] + \rho_m \vec{g} + \vec{F} - \nabla.\left(\sum_{k=1}^{n} \alpha_k \rho_k \vec{v}_{dr,k}\, \vec{v}_{dr,k}\right) \tag{3}$$

where μ_m is the viscosity of the mixture and $\vec{v}_{dr,k}$ is the drift velocity for secondary phase. The gravitational effect was defined as a constant −9.81 m/s², and the thermophysical properties of the air and water phases used in the modeling are presented in Table 1. These parameters are among the key inputs affecting the accuracy of the solution and include characteristics such as density, dynamic viscosity, and specific heat capacity. During the simulation process, the water phase was assigned constant properties by assuming a fixed temperature, while the air phase was modeled using the ideal gas approach. This methodology ensures that interphase interactions and energy transport are represented in a manner consistent with physical reality.

Table 1. Thermophysical properties of the phases [20]

Name of Material	Density (kg/m^3)	Viscosity (kg/ms)	Heat capacity Cp (J/ kg.K)
Air	1.225	1.7894x10^{-5}	1006.43
Water-liquid	998.2	0.001003	4182

The accuracy and stability of numerical analyses largely depend on the geometric definitions and the mesh structure employed. In this context, a three-dimensional geometry was modeled to replicate the experimental setup, and the flow domain was discretized with a mesh structure that balances solution accuracy and computational cost, as illustrated in Figure 4.

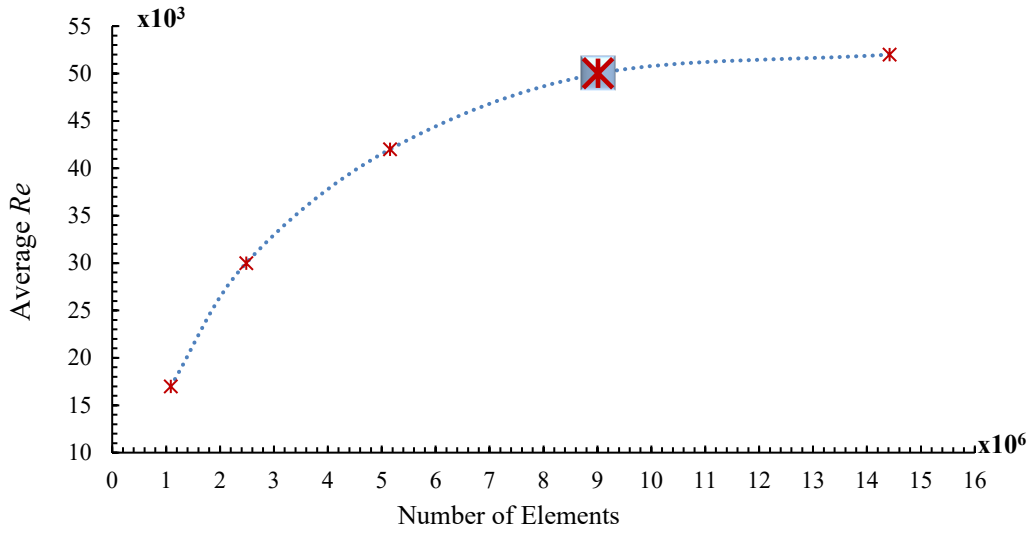

Figure 4. Effect of mesh density on the numerical *Re* number

Figure 5(a) presents the overall mesh structure, while Figure 6(b) illustrates local mesh refinement near the boundary region. To capture the time-dependent effects of turbulence in the numerical modeling, the URANS approach was adopted, with the SST k-ω model selected as the turbulence closure. This model was preferred due to its ability to stabilize turbulence growth near the boundary layer and accurately represent velocity gradients in the subsurface wave regions.

The near-wall mesh resolution was configured to achieve a dimensionless wall distance of $y^+ \approx 1.205$, ensuring the reliability of viscous sublayer resolution and enabling accurate performance of the SST k-ω model under low Reynolds (Re) number conditions. In the 3D model, a quad-dominant mesh structure was employed, with increased cell density near the walls to enhance flow resolution in the boundary layer region. As a result, the y^+ values remained within the targeted range of 1–5 [21], allowing more precise capture of gradients in wave–wall interaction zones.

To replicate the experimental conditions accurately, a time-dependent inlet velocity profile was defined in the numerical model. For this purpose, a user-defined function (UDF) written in C was implemented in ANSYS Fluent 2023 R2 [18]. The inlet boundary conditions of the numerical model were meticulously configured to precisely replicate the piston motion employed in the experimental apparatus. A time-dependent velocity profile was implemented via a User-Defined Function (UDF) as expressed in Equation (4), which accurately reproduces the sinusoidal displacement pattern of the hydraulic servo system (HSS) with identical kinematic parameters (50 mm stroke length and 1 Hz frequency). This methodological approach ensures direct correspondence between the numerical inlet conditions and the real-time motion characteristics of the experimental wave generator. The simulation duration was deliberately constrained to examine the initial wave formation and propagation prior to the occurrence of boundary reflections, thus isolating the primary wave generation physics from secondary reflection phenomena. Consequently, wave reflection effects were not explicitly validated in this investigation, as the focus remained on the immediate hydrodynamic response to the piston's excitation rather than long-duration wave field evolution where reflections become significant.

$$u(t) = \alpha . 2\pi f . \cos(2\pi f t) \tag{4}$$

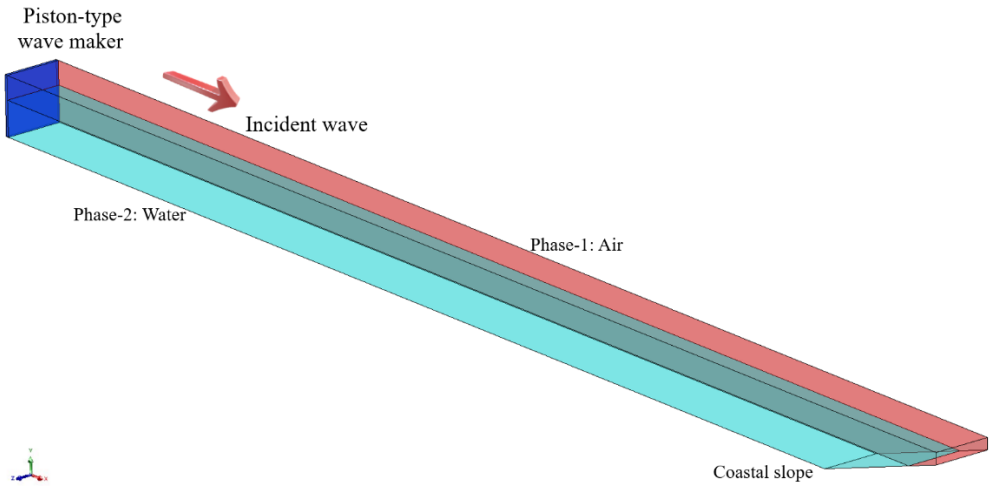

(a)

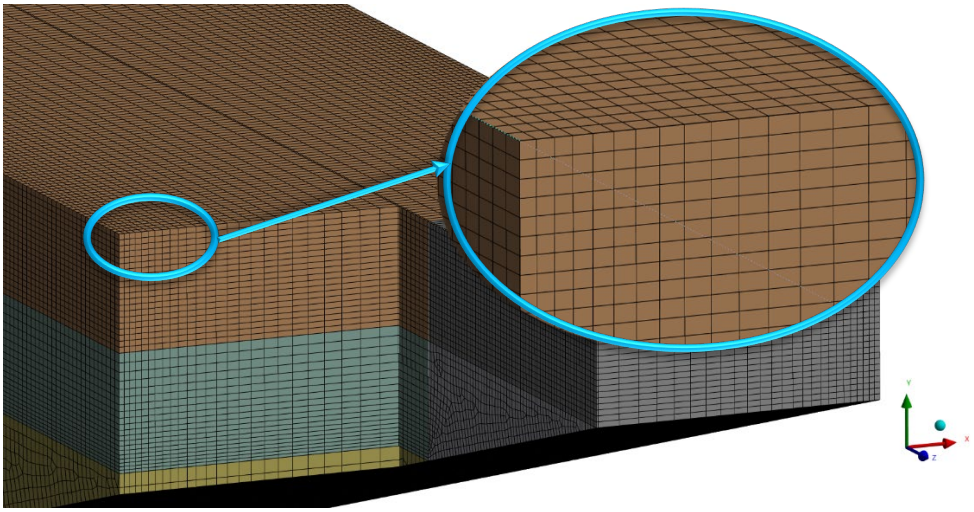

(b)

Figure 5. (a) Two-phase (air–water) numerical wave tank geometry with a piston-type wave generator and a sloped beach; (b) locally refined mesh structure near wall regions suitable for resolving the viscous sublayer.

Here, α denotes the wave amplitude (m), f the frequency (1 Hz), and t the time (seconds). In addition, surface tension effects at the two-phase interface were modeled using a constant surface tension coefficient ($\sigma = 0.0728$ N/m). The calculation of surface tension forces was carried out using the Continuum Surface Force (CSF) model implemented in Fluent. For turbulence modeling, the SST $k-\omega$ model was selected to enable more accurate representation of boundary layer behavior [19]. Furthermore, the UDF was configured to operate in sync with a solution time step of 0.0001 s, updating the inlet velocity at each iteration [19].

2.5. Uncertainty Analysis

A rigorous uncertainty analysis was conducted to ensure the reliability of the experimental wave elevation data, which directly influence the boundary conditions applied in the numerical simulations. Both Type A (random) and Type B (systematic) uncertainties were evaluated, and the combined standard uncertainty was calculated using the root-sum-square (RSS) method as Equation (5) [22-23]:

$$W_T = \sqrt{[(a)^2 + (b)^2 + (c)^2 + (d)^2]} \tag{5}$$

where a denotes the sensor calibration error, b the analog-to-digital conversion resolution, c the ambient thermal drift effect, and d the repeatability deviation across measurements. Additionally, time-resolution uncertainty was quantified Equation (6):

$$W_t = \sqrt{[(e)^2 + (f)^2]} \tag{6}$$

where e represents the data acquisition timing interval uncertainty, and f captures signal delay from digital processing. Based on this approach, the overall uncertainty in wave elevation measurements was determined to be within ±0.5 mm, while timing-related uncertainty remained below ±0.1 s. These values fall within the acceptable range for high-resolution CFD model validation and were used to define confidence bounds on numerical pressure gradient outputs. As seen Table 2, the total combined uncertainty in wave elevation measurements was found to be ±0.715 mm, while the aggregated timing uncertainty reached ±0.022 s. These quantified limits were directly integrated into the numerical model calibration to maintain the fidelity of pressure gradient estimations and to ensure consistency across the CFD validation framework.

Table 2. Uncertainty analysis of wave and flow measurements.

Parameters Causing an Error	Unit	Total error (±)
Wave elevation measurement	mm	±0.715
Time measurement	s	±0.022
Flow velocity (derived from wave data)	m/s	±0.03
Other systematic uncertainties	%	±0.1–0.2
Calibration error (a)	mm	0.20
A/D resolution error (b)	mm	0.61

Environmental drift (c)	mm	0.10
Repeatability error (d)	mm	0.30
Combined elevation uncertainty (W_T)	mm	0.715
Sampling resolution error (e)	s	0.020
FPGA signal delay (f)	s	0.010
Combined timing uncertainty (W_t)	s	0.022
Assumed flow velocity uncertainty	m/s	0.03
Other systematic uncertainties	%	0.1–0.2
Total consolidated uncertainty	–	Wave: ±0.715 mm, Time: ±0.022 s

3. RESULTS AND DISCUSSION

This study presents the numerical solution results of a regular wave field generated by a PTWM controlled via an FPGA-based PI controller. During the experimental phase, wave generation was carried out using different stroke lengths and frequency values. The resulting wave motions were characterized using the Re number, serving as a validation metric for the accuracy of the system. Within the scope of this study, absolute, static, and dynamic pressure fields formed within the channel were investigated in detail. The analyses focused on ∇Ps, subsurface accelerations, and momentum transfer mechanisms occurring during wave generation, propagation, and shoreline impact processes. The distribution of pressure fields throughout the computational domain was evaluated to identify both energy concentration zones and potential load transfer regions.

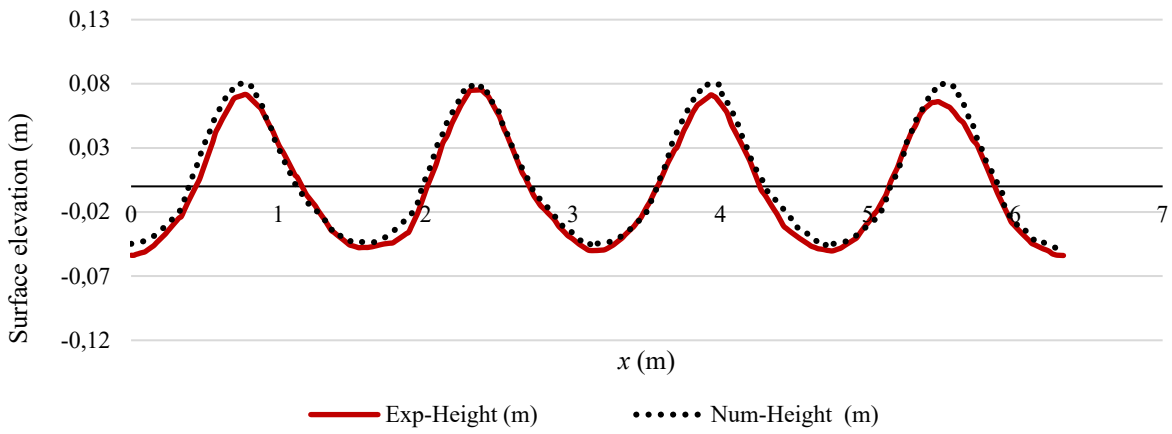

Figure 6. Comparison of experimental and numerical free surface elevations along the wave propagation direction

Figure 6 presents a comparative assessment of experimental and numerical free surface elevations along the wave propagation direction. A significant phase agreement and amplitude similarity are observed between the two profiles, indicating that the numerical model successfully captures the physical characteristics of wave propagation. The numerical model produced, on average, approximately 4.2% higher amplitudes at wave crests compared to experimental measurements. For instance, at the second wave crest, the experimental height was measured at approximately 0.072 m, while the numerical height was calculated as 0.075 m.

Similarly, the numerical data exhibited a slight underestimation of amplitude at the wave troughs relative to the experimental data. This bidirectional deviation trend may result from dispersive effects, the choice of turbulence model, or temporal resolution limitations—even in high-resolution meshes. The overall convergence rate in terms of free surface elevation over the entire wave period was calculated to be approximately 94.04%. This value falls within the ±10% deviation margin commonly accepted in the literature, indicating that the numerical model provides a sufficient level of accuracy [24].

The smoothness and spatial continuity of the wave profile also indirectly validate the numerical solution's stability and the appropriateness of the applied boundary conditions. The minimal phase shift and preserved amplitude further support the correct implementation of the free-surface boundary condition.

Figure 7 presents contour maps of pressure variations induced by wave generation and propagation, evaluated from different pressure components. Figure 7(a) illustrates the distribution of static pressure along the channel. In the computations, gauge pressure was used, with atmospheric pressure (101325 Pa) taken as the reference point. Consequently, regions below atmospheric level exhibit negative static pressure values. These negative values are physically valid and primarily result from wave structures and flow acceleration in the liquid phase beneath the free surface. During wave motion, local pressure drops occur in trough regions and zones of increased velocity due to the Bernoulli effect, which leads to negative gauge pressure values. The recorded values remain well above the cavitation threshold of −99000 Pa, indicating a physically safe operating regime [25].

A pronounced ∇P is observed along the water–air interface, progressing from the inlet region toward the sloped beach, as a result of the periodic wave motion. In particular, the pressure differences at wave crests and troughs vary with time and are directly correlated with wave elevation at the free surface. The gradual decline in the static pressure field also reflects the transfer of momentum carried by the forward-propagating wave toward the shoreline. The pressure profile is notably concentrated near the bottom and decreases toward the surface, indicating the presence of an upward gradient due to hydrostatic pressure effects.

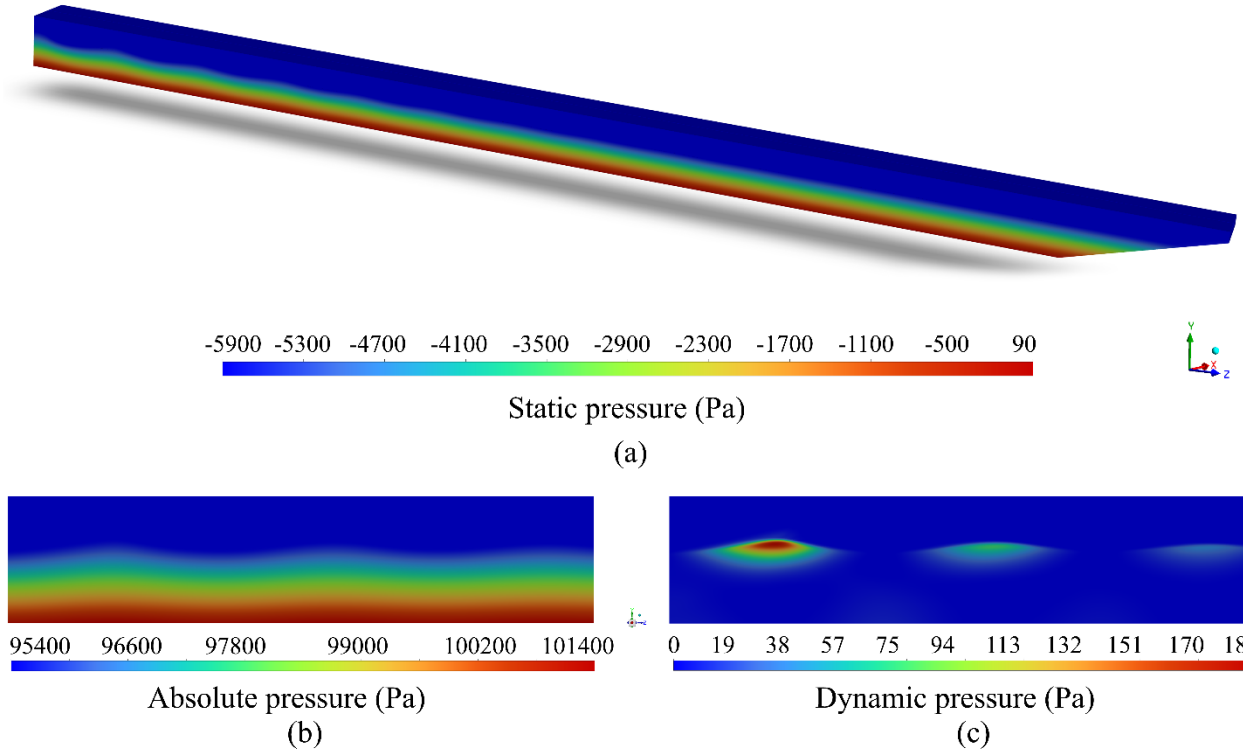

Figure 7. Contour distributions of different pressure types induced by wave–channel interaction: (a) static pressure (isometric view), (b) absolute pressure (right plane), (c) dynamic pressure (right plane)

Figure 7(b) presents the absolute pressure distribution obtained from a cross-sectional view along the right plane. The absolute pressure profile represents the total pressure resulting from the combined modeling of liquid and gas phases. This field, defined by considering both the hydrostatic pressure component and atmospheric conditions, increases notably with depth within the water column. While the values remain relatively low at the surface due to the influence of air, they rise significantly toward the lower sections of the water column demonstrating both the accuracy of the phase transition modeling and the physical consistency of the simulation.

Figure 7(c) shows the distribution of dynamic pressure. In regions where high-energy wave crests pass, localized peaks are formed, indicating abrupt accelerations and effective momentum transfers in the flow. These regions correspond to zones of maximum wave energy and are particularly indicative of velocity-induced pressure increases occurring prior to wave breaking on the sloped beach [19, 26–27].

Figure 8 presents the pressure distribution and ∇P fields developed along the channel as a result of wave formation and propagation following piston motion. Figure 8(a) shows the static pressure values along the bottom of the wave channel in the direction of flow. These values were calculated based on the gauge pressure definition. Since atmospheric pressure was taken as the reference, all sub-surface pressures fall within the negative range. The pressure field generated throughout the 3D wave motion exhibits significant variation near the inlet region due to the influence of high-amplitude waves. In particular, pressure drops occur in regions where wave troughs are concentrated, explained by localized vacuum effects induced by wave crest–trough dynamics under the Bernoulli effect.

Figure 8(b) displays the corresponding ∇P distribution for the same region. This contour clearly reveals the time-dependent behavior of dynamic wave loads and momentum transfer within the flow. Areas of increased gradient intensity identify critical zones dominated by wave breaking and sudden directional changes. These zones are particularly concentrated at the junctions between the channel bottom and sidewalls, in wave crest–trough transition areas, and near the piston outlet section. Sudden velocity and directional shifts induced by wave motion in these regions cause high levels of momentum transfer at boundary surfaces, leading to elevated gradient magnitudes [28].
Figure 8(c) presents the linear projection of wave propagation along the *ZY* plane after piston motion. It illustrates the vertical flow structure within the wave and the pressure distribution of gradients with respect to water column depth. Notably, subsurface return flows and high gradient concentrations near the bottom are observed beneath the surface waves.

Figure 8(d) shows the static pressure distribution throughout the wave channel. It is observed that the system reaches a quasi-steady regime beyond approximately 10 meters. In this region, the static pressure profile becomes more stable, with small-amplitude oscillations. This behavior indicates that the flow structure is well-organized and that wave energy propagates in a controlled manner throughout the channel.

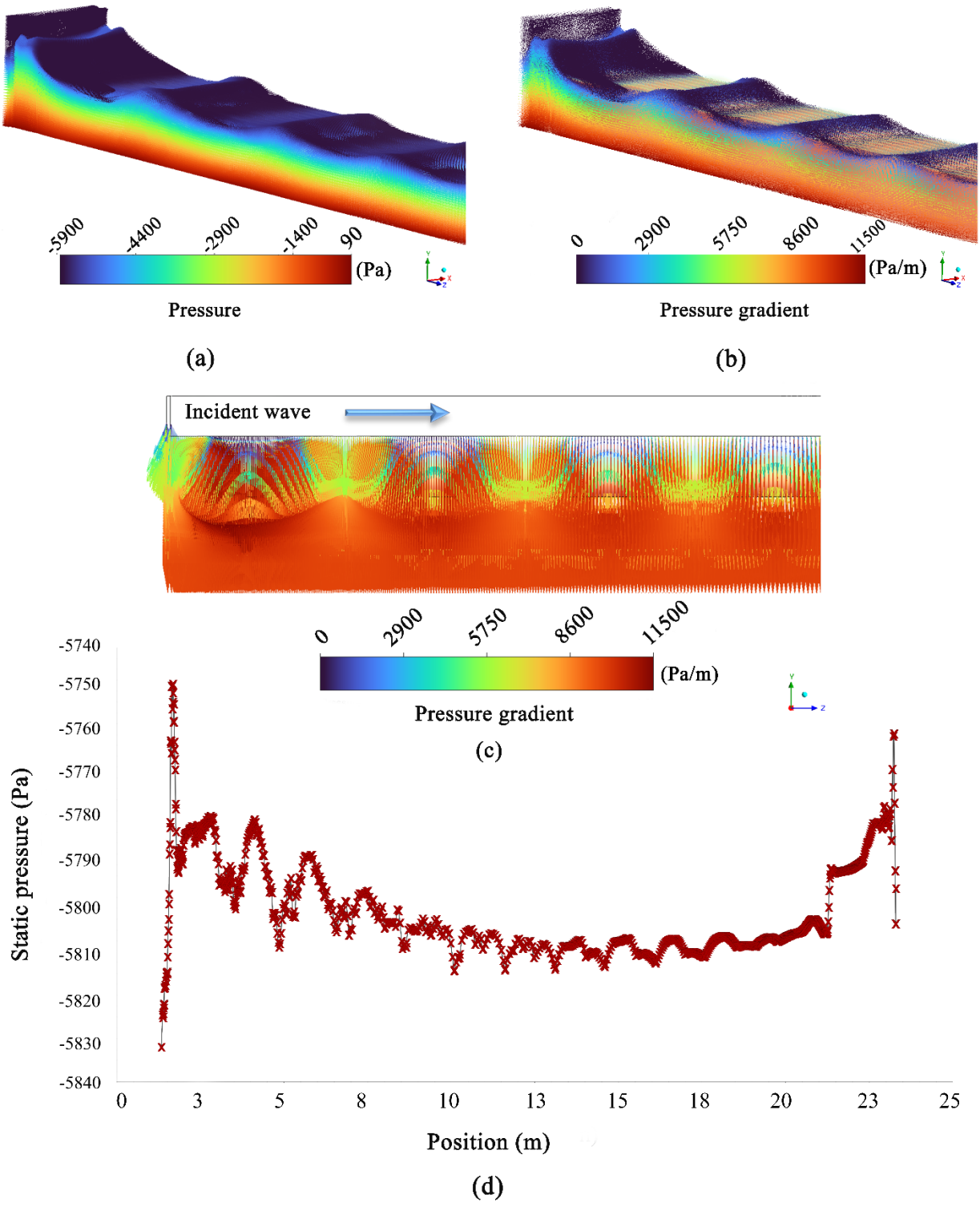

Figure 8. (a) Instantaneous total pressure contour in a 3D isometric view, (b) ∇P distribution from a 3D cross-sectional perspective, (c) ∇P field and wave–crest interaction from a right-plane cross-section, (d) static pressure variation along the z-direction.

4. CONCLUSION

This study encompasses the experimental and numerical evaluation of hydrodynamic and pressure characteristics associated with energy conversion in regular wave fields generated by a piston-type wave generator integrated with an FPGA-based control system. The URANS-based SST k-ω turbulence model employed in the numerical analyses demonstrated a comparable level of accuracy to stabilized turbulence models, particularly in representing high energy concentrations in pre-breaking regions [14–16].

In conventional wave energy analyses, energy flux is typically calculated using free surface parameters such as wave height (H), period (T), and group velocity (C_g). However, this approach estimates energy solely based on surface geometry, neglecting the dynamic structure beneath the water column. In reality, acceleration, momentum transfer, and localized load variations in subsurface regions directly influence where energy is concentrated and how it is transported toward the shoreline [28]. As a result, even in systems with identical wave heights, different flow structures may lead to varying spatial distributions of energy intensity.

In this study, the ∇P, static pressure, and dynamic pressure contours clearly revealed the temporal and spatial localization of wave energy. The presented analyses particularly demonstrate how pressure fields represent critical components of energy transfer events, including subsurface load distribution, wave breaking, and momentum exchange.

These parameters are crucial for the optimal placement of WECs, mechanical load estimation, and efficiency analysis. As emphasized in the literature, performance evaluation of energy conversion systems should not rely solely on free surface elevations, but must also account for subsurface pressure fields and velocity gradients [11–12,14].

The holistic pressure-based analytical approach proposed in this study extends beyond classical wave analyses and contributes to the development of engineering decision-support frameworks aimed at enhancing the physical accuracy of subsystems involved in wave energy conversion [26]. The findings demonstrate strong agreement with similar studies in the literature, both in terms of experimental validation and numerical solution stability [10,19,28]. Accordingly, FPGA-based control systems integrated with piston-type wave generators offer a physically accurate, stable, and practically feasible solution for improving wave energy conversion efficiency.

This study contributes meaningfully to the literature through the high-fidelity numerical resolution of subsurface pressure gradients in regular wave fields. As a natural extension of the current research, a systematic parametric sweep in the frequency–amplitude domain (0.5–2.0 Hz; 25–100 mm) could enable comprehensive spectral mapping of energy concentration zones. Under irregular wave conditions, the application of JONSWAP and Pierson–Moskowitz spectra would allow for probabilistic assessments of pressure–momentum transfer and energy conversion efficiency. Furthermore, the quantification of hydrodynamic damping and radiation–diffraction effects induced by the presence of wave energy converters (WECs) represents a critical direction for future investigation. From a methodological standpoint, the integration of high-speed Particle Image Velocimetry (PIV) and Laser-Induced Fluorescence (LIF) techniques can facilitate synchronized measurements of sub-surface flow structures and turbulence dynamics. These experimental advances would support the development of hybrid LES/RANS frameworks that span micro-scale turbulence phenomena to macro-scale wave propagation. Ultimately, constructing fully coupled wave energy converter models that integrate hydrodynamic, electromagnetic, and structural mechanics subsystems will provide a robust theoretical foundation for performance optimization and next-generation design of marine energy systems.

NOMENCLATURE

T	Wave period (s)
y^+	Dimensionless wall distance
Greek Symbols	
α	Wave amplitude (m)
f	Frequency (Hz)
g	Gravitational acceleration (m/s^2)
p	Pressure (Pa)
t	Time (s)
∇P	Pressure gradient (Pa/m)
μ	Dynamic viscosity (kg/m.s)
ρ	Density (kg/m^3)
σ	Surface tension coefficient (N/m)
ω	Specific dissipation rate (1/s)
Subscripts	
avg	Average value

max	Maximum value
min	Minimum value
Abbreviations	
CFD	Computational Fluid Dynamics
CSF	Continuum Surface Force
FPGA	Field Programmable Gate Array
H	Wave height
HSS	Hydraulic Servo System
LVDT	Linear Variable Differential Transformer
PDV	Proportional Directional Valve
PTWM	Piston-Type Wave Maker
Re	Reynolds number
SST	Shear Stress Transport
UDF	User-Defined Function
URANS	Unsteady Reynolds-Averaged Navier-Stokes
VOF	Volume of Fluid
WEC	Wave Energy Converter

DECLARATION OF ETHICAL STANDARDS

The authors declare that this study complies with the ethical standards of scientific research.

CONTRIBUTION OF THE AUTHORS

Altug Yavas: Writing, methodology

Batın Demircan: Conceptualization, methodology, validation, formal analysis, investigation, resources, data curation, writing, visualization

Gulenay Alevay Kilic: Conceptualization, methodology, software, validation, formal analysis, investigation, data curation, writing, visualization

Nuray Gedik: Writing, methodology

All authors have read and agreed to the published version of the manuscript.

CONFLICT OF INTEREST

There is no conflict of interest in this study.

REFERENCES

[1] Zullah MA, Prasad D, Ahmed MR, Lee YH. Performance analysis of a wave energy converter using numerical simulation technique. Sci China Technol Sci 2010; 53(1): 13-18.

[2] Gao H, Li B. Establishment of motion model for wave capture buoy and research on hydrodynamic performance of floating-type wave energy converter. Polish Maritime Research 2015; 22(s1): 106-111.

[3] Rajapakse G, Jayasinghe S, Fleming A. Power smoothing and energy storage sizing of vented oscillating water column wave energy converter arrays. Energies 2020; 13(5): 1278.

[4] Carreno-Luengo H, Camps A. Empirical results of a surface-level GNSS-R experiment in a wave channel. Remote Sensing 2015; 7(6): 7471-7493.

[5] Maria-Arenas A, Garrido AJ, Rusu E, Garrido I. Control strategies applied to wave energy converters: state of the art. Energies 2019; 12(16): 3115.

[6] Jusoh MA, Ibrahim MZ, Daud MZ, Albani A, Yusop ZM. Hydraulic power take-off concepts for wave energy conversion system: a review. Energies 2019; 12(23): 4510.

[7] Giannini G, Rosa-Santos P, Ramos V, Taveira-Pinto F. On the development of an offshore version of the CECO wave energy converter. Energies 2020; 13(5): 1036.

[8] Guo B, Ringwood JV. A review of wave energy technology from a research and commercial perspective. IET Renewable Power Generation 2021; 15(14): 3065-3090.

[9] Marques Machado FM, Gameiro Lopes AM, Ferreira AD. Numerical simulation of regular waves: optimization of a numerical wave tank. Ocean Engineering 2018; 170: 89-99.

[10] Velioglu Sogut D, Sogut E, Farhadzadeh A. Interaction of a solitary wave with an array of macro-roughness elements in the presence of steady currents. Coastal Engineering 2021; 164: 103829.

[11] Larsen BE, Fuhrman DR. Simulation of cross-shore breaker bar development utilizing a stabilized two-equation turbulence model. Coastal Engineering 2023; 180: 104269.

[12] Yin Z, Yang G, Wang Y, Qiu Q, Jiang X. Numerical simulations of breaking wave propagation through the vegetation on a slope based on a drag coefficient prediction model. Ocean Engineering 2024; 291: 116440.

[13] Li Y, Larsen BE, Fuhrman DR. Reynolds stress turbulence modelling of surf zone breaking waves. J Fluid Mech 2022; 937: A7.

[14] Chen F, Duan D, Han Q, Yang X, Zhao F. Study on force and wave energy conversion efficiency of buoys in low wave energy density seas. Energy Conversion and Management 2019; 182: 191-200.

[15] Zeinali S, Wiktorsson M, Forsberg J, Lindgren G, Lindström J. Optimizing the hydraulic power take-off system in a wave energy converter. Ocean Engineering 2024; 310: 118636.
[16] Blaser A, Benamran R, Bôas ABV, Lenain L, Pizzo N. Momentum, energy and vorticity balances in deep-water surface gravity waves. J Fluid Mech 2024; 997: A55.
[17] Sumer BM, Kirca VO. Flow through the Bosphorus. Journal of Waterway, Port, Coastal, and Ocean Engineering 2025; 151(3): 04025010.
[18] Mattson JE. An introduction to Ansys Fluent 2022, Sec. Cavitation Modeling. SDC Publications, First Ed., Mission, Kansas, USA, 2022, Ch. 6, pp. 123-141.
[19] Yamaç HI, Koca A, Yılmaz T. Using computational fluid dynamics for wave generation and evaluation of results in numerical wave tank modelling. Firat University Journal of Experimental and Computational Engineering 2022; 1(1): 31-42.
[20] Kaya S, Kuscuoglu A, Kilic GA. Structural safety assessment of a piston-type wavemaker under varying frequency and stroke conditions. Results in Engineering 2026; 31: 111580.
[21] ElCheikh A, ElKhoury M. Effect of local grid refinement on performance of scale-resolving models for simulation of complex external flows. Aerospace 2019; 6(8): 86.
[22] Kilic GA, Yalcin E, Aydin AA. Optimum operating temperature range of phase change materials used in cold storage applications: a case study. In: Dincer I, Colpan C, Ezan M (eds) Environmentally-Benign Energy Solutions. Green Energy and Technology. Springer, Cham, 2020.
[23] Kilic GA, Yalcin E, Aydin AA. Experimental analysis of a cold store integrated with phase change material: a case study. Bulgarian Chemical Communications 2016; 48: 195-198.
[24] Kowalewski TA. Validation problems in computational fluid mechanics. Computer Assisted Mechanics and Engineering Sciences 2011; 18: 39-52.
[25] Castro-Orgaz O, Chanson H. Bernoulli theorem, minimum specific energy, and water wave celerity in open-channel flow. Journal of Irrigation and Drainage Engineering 2009; 135(6): 773-778.
[26] Jusoh MA, Ibrahim MZ, Daud MZ, Yusop ZM, Albani A. An estimation of hydraulic power take-off unit parameters for wave energy converter device using non-evolutionary NLPQL and evolutionary GA approaches. Energies 2020; 14(1): 79.
[27] Silva D, Rusu E, Soares CG. Evaluation of various technologies for wave energy conversion in the Portuguese nearshore. Energies 2013; 6(3): 1344-1364.
[28] Santos Lopez Gutierrez J, et al. Wave energy conversion through oscillating water columns: a review. Journal of Marine Science and Engineering 2024; 12(2): 342.